Paper ID: ETC2023-215

Proceedings of 15th European Conference on Turbomachinery Fluid dynamics & Thermodynamics
ETC15, April 24-28 2023; Budapest, Hungary

CFD STUDY OF THE LEAKAGE FLOW IN LOW-SPEED AXIAL-FAN WITH ROTATING SHROUD

Edward Canepa, Andrea Cattanei, Mohammad Amir Neshat

DIME-Department of Mechanical, Energy, Management and Transport Engineering, University of Genoa, Montallegro, 1, I-16145 Genova, Italy,

mohammadamir.neshat@edu.unige.it

ABSTRACT

The paper reports a study of the effect of the rotational speed on the leakage flow development in a low-speed shrouded axial fan. As the rotor deforms due to centrifugal force and aerodynamic loading, a static structural analysis has been operated at five rotational speeds ranging from 500 to 3000 rev/min, with the pressure distributions on the rotor surfaces derived from RANS-based CFD simulations alternating with FEM ones. Once convergence has been reached, both the structural and aerodynamic results have been validated through available experimental data. Then, the deformed geometries related to two rotational speeds, 2400 rev/min and 3000 rev/min respectively, have been used to perform URANS CFD simulations and then to analyze the effects of the different gap geometries on the leakage flow behavior. The results have allowed interpreting the behavior of the leakage flow evolving in the gap between the rotating shroud and the stationary casing.

KEYWORDS

Axial-flow fan, rotating shroud, leakage flow, rotor deformation.

NOMENCLATURE

G	moment of momentum flux
Q	volume flow rate
r	radial coordinate
x	position vector
Tu	turbulence intensity based on u_{tip}
u_{tip}	peripheral speed of the blade
u_τ	friction velocity
v_a, v_r, v_θ	non dimensional components of the absolute velocity
v_m	non dimensional component of the absolute velocity in a meridional plane
x	axial coordinate
y^+	non-dimensional wall distance, $\frac{u_\tau y}{v}$
z_R	rotor blade number
Δp	pressure rise through the rotor (static outlet minus total inlet)
ρ_0	air density
φ	flow coefficient, $\frac{Q}{u_{tip}\pi r_{tip}^2}$

ψ pressure rise coefficient, $\frac{\Delta p}{0.5\rho_0 u_{tip}{}^2}$

Ω rotational speed (expressed in rev/min)

Superscripts

$\sim$ related to the periodic phenomenon

$-$ related to the time average

$'$ related to non-periodic instantaneous fluctuations

Subscripts

hub   related to hub

tip   related to the blade tip

INTRODUCTION

Low-speed axial-flow fans are commonly employed for civil, industrial, and transportation applications. In many cases, the constraints on performance are less important than the ones on encumbrance, simplicity, or cost per unit. Therefore, cheap, low stiffness materials are often adopted that result in important deformations when the rotors operate, Gokpi et al. (2018). In order to reduce the yielding drawbacks, the rotors are often provided with a rotating shroud (a kind of ring) that improves the volumetric efficiency, Longhouse (1978); such a ring strengthens the whole rotor assembly, thus allowing the adoption of highly swept blades, which constitute a quite effective solution to reduce the generated noise. Anyway, this solution yields a leakage flow evolving through the stationary casing and the ring, whose typically reported effect is an increase in the radiated noise due to the presence of large-scale turbulent structures. Namely, their interaction with the rotor blades generates noise in the low- to medium-frequency range, with the appearance of narrowband humps at subharmonic frequencies and a general increase of the broadband noise, Piellard et al. (2014) and Zhu et al. (2015). The complexity of both geometry and flow prevents from taking exhaustive aerodynamic measurements in the gap zone and also makes numerical simulations challenging. Only recently, detailed unsteady numerical studies have been performed, e.g.: Magne et al. (2012), Zayani et al. (2012), Piellard et al. (2014), Magne et al. (2015) and Ghodake et al. (2022). These works have been mainly focused on directly simulating the emitted noise while the aerodynamic aspects of the flow in the gap zone have not been deepened.

The blade deformation is strongly reduced by the ring, but a residual axial displacement of the ring usually remains. The related effects on the leakage flow pattern have been experimentally studied, e.g. see Canepa et al. (2019), while very few studies on rotor deformation of shrouded axial fans have been found in the literature, e.g. Moreau et al. (2000), Henner et al. (2009), and Nouri et al. (2010). However, none of them regards the effects of the leakage flow on the main one.

The present paper constitutes a numerical investigation focused on the same geometry experimentally surveyed in Canepa et al. (2016, 2018 and 2019) and is based on a preliminary fluid-structure interaction (FSI) analysis applied through a one-way coupling method. The combined effect of the centrifugal force and the pressure distribution modifies the fan geometry, but no flutter is present since the power associated to the deformation is negligible. Therefore, the undeformed geometry has been used to obtain an initial pressure distribution on the rotor surfaces allowing the evaluation of a deformed geometry through a FEM analysis. Such a new geometry has been used for the final CFD simulation, since convergence has been immediately achieved. Then, the obtained deformed geometry has been validated based on experimental results related to different rotational speed and same non-dimensional flow rate and pressure rise. Once validated, the resulting flowfields

have been analyzed with particular attention to the gap zone and focusing on the development of the leakage flow inside the gap and upstream of the rotor.

NUMERICAL SETUP

Fan geometry, numerical domain, and meshing process

The considered geometry consists of a low-speed axial fan with $z_R = 9$ evenly spaced, forward swept blades, Fig. 1. The rotor is provided with a rotating shroud of external diameter of 460 mm; the blade tip radius is $r_{tip} = 227$ mm, the hub radius is $r_{hub} = 90.5$ mm and the blade chord c varies between 65 mm at the hub and 72 mm at the tip, which correspond to an axial chord of 27 mm and 15 mm, respectively. The stagger angle, defined as the angle between the chord and the axial directions, ranges between 65.2 deg at the hub and 75.8 deg at the tip.
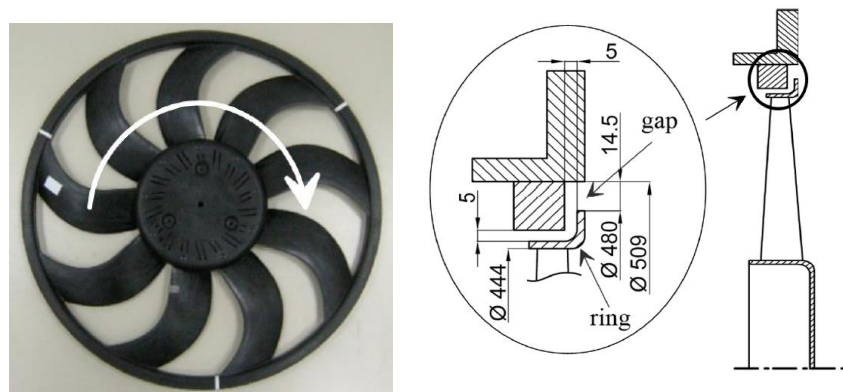

Figure 1: Rotor prototype and gap geometry.

The rotor and gap geometries are shown in Fig. 1. The fan has been mounted on a rectangular wooden panel (690x710 mm, 25 mm thick) with the rotor axis located at the height of 1.15 m from the floor. In order to vary the operating point, a test-plenum, realised according to ISO 10302, has been employed (1010x1210x1405 mm) and a rectangular duct has been inserted between it and the wooden panel. The test plenum is provided with two back slots (920 x 280 mm each) which allow to continuously vary the discharge area and the operating points during the measurement campaigns. The design performances are a flow rate $Q = 1.174$ m^3/s and a static pressure rise $\Delta p = 388$ Pa at the rotational speed $\Omega = 3000$ rev/min with air at ambient conditions 293.15 K, 101300 Pa). This results in a flow coefficient $\varphi = Q/(u_{tip}\pi r_{tip}^2) = 0.098$ and a pressure coefficient $\psi = \Delta p/(0.5\rho_0 u_{tip}^2) = 0.121$ where u_{tip} is the blade tip speed. Other details of the fan and of the test configuration are reported in the experimental study of Canepa et al. (2018). At $\Omega = 3000$ rev/min, the Reynolds number based on the relative velocity at the rotor inlet, and on the blade chord length is $Re_{tip} \approx 3.45$ x 10^5 at the tip (the kinematic viscosity equals 1.5x10^{-5}) and $Re_{hub} \approx 1.29$ x 10^5 at the hub.

The simulated geometry is reported in Fig. 2 and is composed by an upstream hemisphere, the rotor and the test plenum. The geometrical details on the numerical domain have been kept similar to the real one apart from some irrelevant aspects of the motor. The rotating domain is enveloped by an interface surface with imprinted connectivity. Both rotating and stationary domains have been discretized using polyhedral unstructured mesh which has been found suitable for complex geometries (as the gap one) and allows reducing the required computational resources, Jasak et

al. (2020). The meshing process, as well as the numerical simulations, have been performed by means of the commercial suite Star-CCM+. A prism layer discretization has been adopted and characterized by 20 layers with a total thickness of 0.7 mm; the adopted growth rate is equal to 1.1 leading to an inner cell height lower than 0.02 mm hence allowing the wall y^+ to limits to values close to unity.
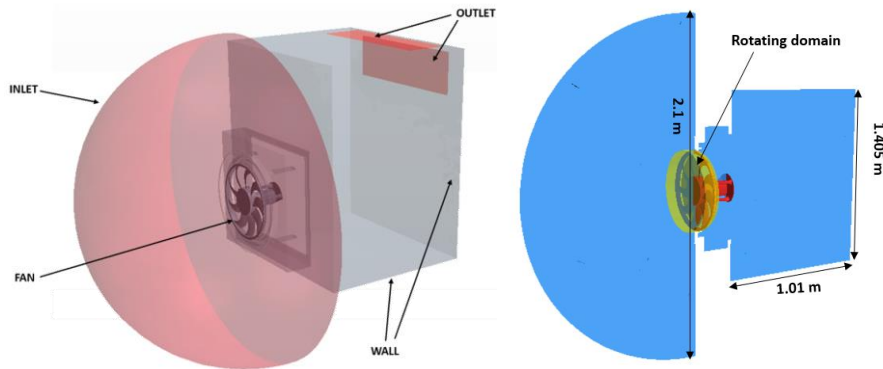

Figure 2: Computational 3D domain and a meridional section.

Physical model and boundary conditions

The FSI simulation requires the surface pressure distribution on the fan, which is scarcely influenced by the unsteady phenomena related to the leakage flow, Canepa et al. (2018). Hence, the RANS approach has been adopted for the FSI instead of the URANS one, thus yielding an important simplification.
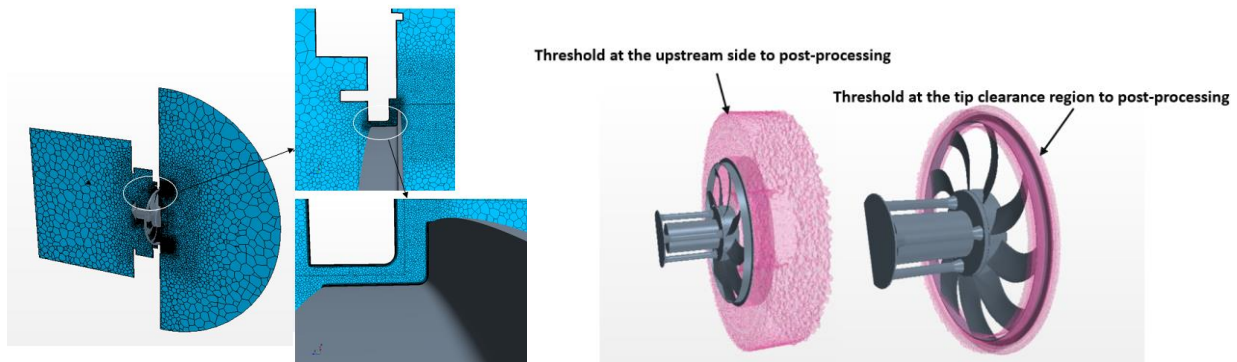

Figure 3: Examples of the adopted mesh and the exported sub-domains.

Differently, in order to properly simulate the leakage flow (namely mixing process with the main flow and insurgence of large vortical structures) the URANS equation set has been employed once the deformed geometry has been obtained and the related grid generated. At the maximum rotational speed, 3000 rev/min, the peripheral speed of the blade tip is $u_{tip} = 70.2$ m/s, which leads to a tip Mach number lower than 0.3. Therefore, the density has been considered constant and a segregated SIMPLE-type algorithm has been used for simulations.

The use of two-equation models is well established within the industrial fan community to solve the RANS closure problem, e.g. see Corsini et al. (2013). The Menter's k-ω SST turbulence model has been adopted since the boundary layer development is of particular importance on the rotor blade and in the gap zone, while large turbulent structures may develop in the leakage flow, e.g. see Moreau et al (2006) and Romik (2022); it solves the equation for ω near the wall and for ε elsewhere hence allowing to use the best features of the two models.

On the inlet hemisphere, a uniform normal velocity has been imposed to obtain the desired flow rate, while the standard atmospheric pressure has been fixed on the outlet surfaces. For all the remaining surfaces, a no-slip condition has been used. The evolving fluid is air, and the reference temperature is fixed at 288.15 K, leading to a density equal to 1.184 kg.m^{-3} and a dynamic viscosity equal to 1.855×10^{-5} kg m^{-1}s^{-1}.

In the URANS simulations, a second-order temporal scheme has been chosen and in order to properly characterize the convective phenomena the Courant number (CFL) criterion has been adopted and used to identify a suitable time step. It has been found that discretizing the blade passing period in 110 points resulted in a CFL lower than unity in the gap zone. Five full revolutions have been simulated. To determine the fan deformation, a tetrahedral mid side node mesh has been used in the FEM simulation where the number of cells has been identified through a sensitivity analysis based on the Von Mises stress. The final mesh is composed by $3x10^5$ cells. The fan material mechanical properties are: density 1320 kg/m^3, Young's modulus 3.5×10^9 Pa, Poisson's ratio 0.4.

Methodology

Since the impact of the leakage flow pattern modification on the overall performance is small, the undeformed geometry has been used for the CFD mesh sensitivity analysis. Varying the mesh base size, several grids have been generated with an overall cell number ranging from $4.6x10^6$ to $20x10^6$ and the RANS model has been used. The rotational speed has been set to 3000 rev/min and the resulting pressure rise has been monitored. It has been found that, from $9.7\ x10^6$ cells on, the pressure rise does not vary considerably with a difference from the experimental one of nearly 2.5%. Hence, such a grid has been adopted.

The static structural analysis (SSA) has been performed at fixed operating point (φ=0.098) and at five rotational speeds ranging from 500 to 3000 rev/min (for each case, the inlet velocity has been evaluated consistently with the condition that φ=0.098). The rotor surface pressure distributions derived from the steady CFD simulations have been exported and interpolated on the FEM mesh, hence allowing to compute the deformed geometry. In the Ω=2400 and Ω=3000 rev/min cases the deformed geometries have been re-introduced in the CFD simulation and it has been found that a new FEM computation would not result in any further deformation. This aspect is consistent with the findings of Moreau et al. (2000) and Canepa et al.(2018), since it has been found that the centrifugal forces constitute the dominant load on the blade.

The major effect of the deformation, which will be analyzed more in detail way in the result discussion section, is a few-millimeter axial displacement of the ring, which leaves the blade geometry nearly unmodified. On the contrary, even slight variations of the gap geometry are important and may affect largely the leakage flow pattern. Successively, in the Ω=2400 rev/min and Ω=3000 rev/min cases, the deformed fan geometries have been used to perform the unsteady CFD simulations, thus allowing to analyze the effects of the different gap geometries on the leakage flow behavior.

Post-processing

The experimental analysis reported in Canepa et al. (2018 and 2019), as well as the numerical ones reported in Moreau et al. (2016), indicate the presence of large scale vortical structures that may develop in the leakage flow or may be generated upstream of the rotor by its interaction with the main one. Depending on the generation mechanism, these structures may be periodic or not. Hence, a phase averaging technique has been employed to separate the different characteristics of the flowfield. To apply this technique, the instantaneous solution has been exported and interpolated using a linear scatter interpolation method. Particularly, two sub-domains have been chosen (Fig. 3) basing on their importance on the leakage flow development: one related to the rotor zone and the other focused on the gap area. Considering that the rotor hub rear section corresponds to the zero of the absolute reference system, the former domain extends in axial direction from 0.8 r_{tip} upstream to 0.15 r_{tip} downstream, with a radial range equal to 0.4 < r/r_{tip} <1.71. The latter domain has an axial extension of 0.18 r_{tip} across the gap and ranges in the interval 0.97 < r/r_{tip} <1.155 in the radial direction. To avoid excessive computational efforts, the exporting process has been performed every five time-steps, which results in a 22-points discretization of the blade passing period. Two full rotor revolutions have been considered. The interpolation grids have overall dimensions slightly smaller than the exported domains ones and a similar spatial resolution.

According to the triple decomposition scheme proposed by Hussain and Reynolds (1970) for the study of coherent structures, a generic velocity component v at a generic position $\mathbf{x}$ can be represented as the sum of the time mean contribution $\bar{v}$, the zero-average periodic component $\Delta\tilde{v}$ and the fluctuating part v' accounting for the departure of the instantaneous flow field from the periodic one: $v(\mathbf{x}, t) = \bar{v}(\mathbf{x}) + \Delta\tilde{v}(\mathbf{x}, \phi) + v'(\mathbf{x}, t)$. For present simulations, the main source of periodicity is the rotor revolution; thus, at generic time instant t, $\Delta\tilde{v}$ may be related to a specific angular position, i.e. to the phase $\phi = \phi(t) = 2\pi\Omega t/60$ of the periodic phenomenon. Performing the averaging procedure in the relative frame of reference allows computing $\tilde{v} = \bar{v} + \Delta\tilde{v}$, which represents the time-mean velocity at fixed position in the relative frame. Differently, $\bar{v}$ may be computed as time mean at fixed position in the absolute frame of reference. Hence, v' may be computed subtracting, from the instantaneous value $v(\mathbf{x}, t)$, $\tilde{v}$ corresponding to the effective position of the rotor.
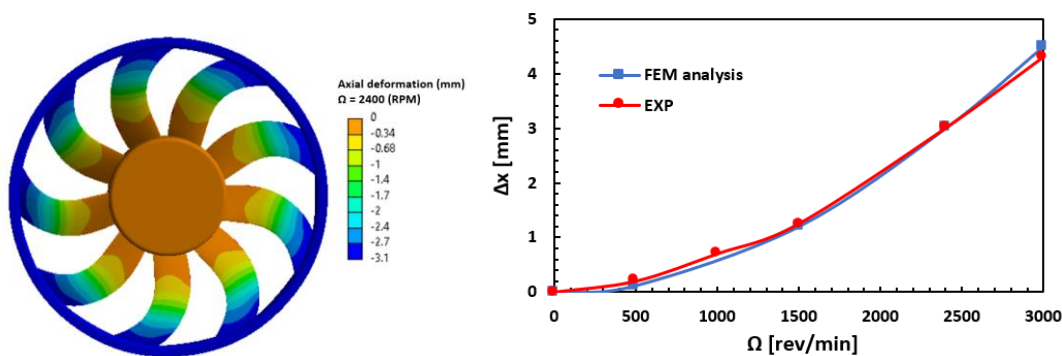

Figure4: Example of FEM results and axial displacement of the rotating shroud as a function of the rotational speed.

Validation

The validation of the FEM results has been performed through the comparison with the data reported in Canepa et al. (2018) where the axial displacement of the rotating shroud has been

measured during a speed ramp characterized by constant φ and ψ equal to those of the present work. The results are reported in Fig. 4 and indicate a very good agreement between the experimental curve and the numerical one. Moreover, an example of the axial displacement of the entire rotor at $\Omega = 2400$ rev/min has been added in the same figure. For $r/r_{tip} <0.8$ the axial displacement of the rotor blades is limited to 2 mm, hence indicating that the blade shape is not strongly altered by the deformation. Differently, the gap discharge section, which in the undeformed configuration is characterized by a 5-mm axial opening (Fig. 1) between the rotating shroud and the stationary casing with the rotor flush mounted on the external panel, is highly affected by the axial displacement. The shroud moves upstream of more than 4 mm in the $\Omega = 3000$ rev/min case.

The CFD results have been validated through the comparison with the mean velocity profiles reported in Canepa et al. (2018), reported in Fig. 5. The surveyed points are located upstream of the fan ($x = 0.044 \, r_{tip}$) in the range $0.529 \leq r/r_{tip} \leq 1.233$ and the velocity components have been made non dimensional by means of u_{tip}.
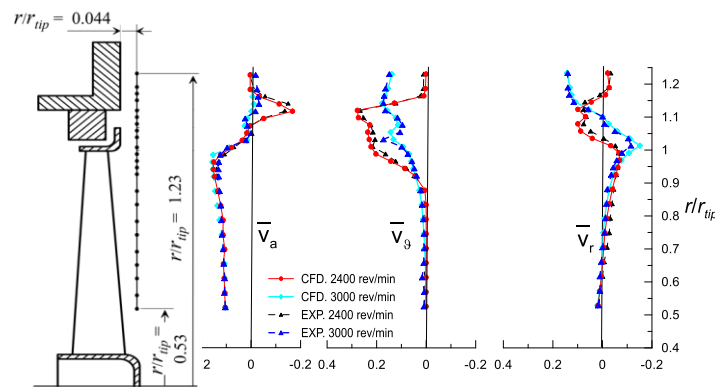

Figure 5: Radial profiles of the mean axial, tangential, and radial velocity components upstream of the fan.

For all the three mean velocity components in the two cases, the numerical results are capable to properly simulate the real case with limited differences. For $\Omega = 3000$ rev/min the axial component is slightly underestimated in the range $0.8 < r/r_{tip} <1$, while for $\Omega = 2400$ rev/min the tangential component is slightly overestimated in the range $0.9 < r/r_{tip} <1.1$. Such small differences may be ascribed to the uncertainties related with the CFD simulations. As a general remark, it should be considered that, in the main flow drawn from the ambient, no pre-rotation may be present; hence, $\bar{v}_\theta > 0$ indicates the presence of the leakage flow leaving the gap and being re-ingested by the fan.

RESULTS AND DISCUSSION

The instantaneous q-factor iso-surfaces in the gap region are represented in Fig. 6 for the two cases, together with the streamlines and the contour of the axial velocity component. The streamline originating points are located on the represented meridional plane and hence the departure from the meridional plane can only be ascribed to the tangential velocity component present in the leakage flow. In the $\Omega = 2400$ rev/min case as the leakage flow leaves the gap and is immediately re-ingested by the fan, the zone characterized by $v_\theta > 0$ is limited to the range $0.9 < r/r_{tip} <1$. This is consistent with the q-factor iso-surface, which properly identifies the separation bubble.

In the $\Omega = 3000$ rev/min case, the separation bubble is present at radial positions larger than r_{tip}, as a consequence the mixing process between the leakage flow and the main one is enhanced, and the

portion of the inlet flow characterized by $v_\theta > 0$ reaches approximately midspan. The fact that the q-factor iso-surface curls indicate the presence of coherent structures laying on the bubble interface suggests that vortical structures are developing in the flow field even at locations different from the separation bubble.
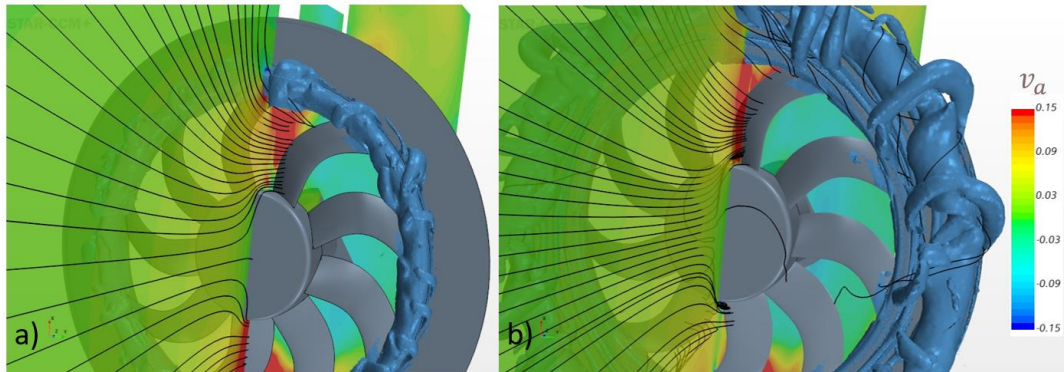

Figure 6: Instantaneous axial velocity component contour on a meridional plane with superposed streamlines and *q*-factor iso-surfaces, a) Ω =2400 rev/min, b) Ω =3000 rev/min

The different characteristics of the two flow fields may also be inferred from the $\bar{v}_\theta$ contour plots reported in Fig. 7. The contours are represented on the meridional plane together with the meridional streamlines. In the Ω =2400 rev/min case, the leakage flow leaves the gap and suddenly bends toward the fan inlet yielding the aforementioned recirculation bubble, which develops along the rotating shroud upstream edge.
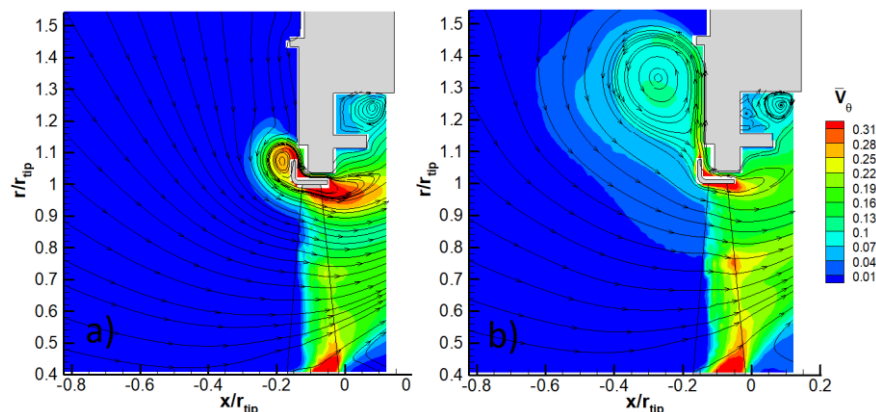

Figure 7: Mean tangential velocity component contour on a meridional plane with superposed streamlines based on the meridional velocity, a) Ω =2400 rev/min, b) Ω =3000 rev/min.

The leakage flow is characterized by $\bar{v}_\theta \cong 0.3$ but when it impinges on the blade leading edge the values reduce to $\bar{v}_\theta \cong 0.2$. The perturbated zone has an axial extension equal to x/r_{tip} =0.15 from the rotating shroud and is confined in the range $0.85 < r/r_{tip} < 1.2$ in the radial direction. In the Ω =3000 rev/min case, the size of the recirculation bubble is extremely enlarged as the leakage flow leaves the gap in radial direction and follows a longer path before being reingested. The $\bar{v}_\theta > 0$ zone extends beyond r/r_{tip} =1.5 and arrives to r/r_{tip} =0.75, while its axial size is larger than x/r_{tip} =0.45. In

the gap discharge section, $\bar{v}_\theta$ has lower values than in the other case and, along the blade leading edge, $\bar{v}_\theta$ is generally lower but the perturbated area has a larger radial extension.
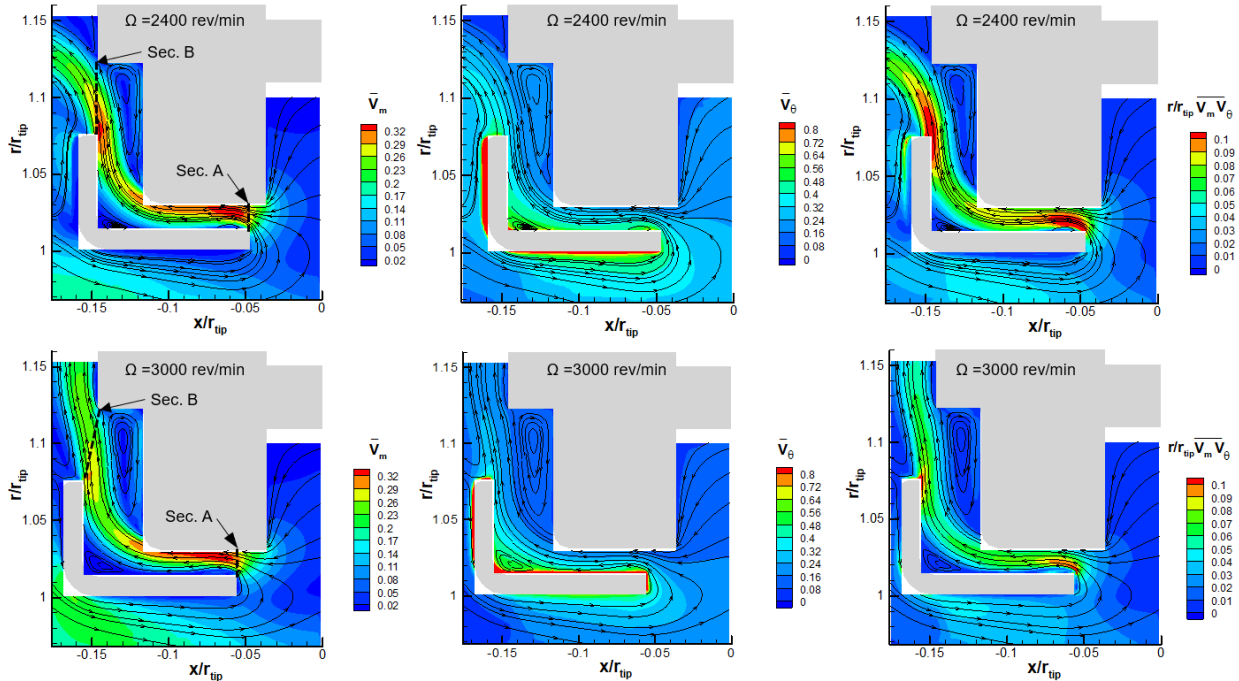

Figure 8: Meridional contours of mean meridional and tangential velocity components, and specific flux of moment of momentum with streamlines.

In order to get better insight into the flow field features in the gap area, the detailed $\bar{v}_m$ and $\bar{v}_\theta$ contour plots are reported in Fig. 8. In the two cases, the gap flow is partially fed from the flow leaving the rotor, which bends around the rotating shroud downstream edge, and the second contribution is constituted by a portion of centripetal flow recirculating along the panel downstream side. To evaluate the flow rate and moment of momentum flux through the gap, the inlet and discharge sections of the gap region (indicated as sec. A and B respectively in Fig. 8) have been considered. The flow rate computed in section A indicates that the leakage flow rate is substantially even at the two rotational speeds and equal to 8.7% of the overall fan flow rate. Once within the gap, the flow strongly accelerates in the upstream direction (large $\bar{v}_m$ values in the ranges $1.02 < r/r_{tip} < 1.03$ and $-0.1 < x/r_{tip} < -0.05$) due to presence of a small separation bubble located on the rotating shroud close to the downstream edge. Moving toward section B, the leakage flow experiences a 90-deg bend induced by the gap geometry, which also generates two separation bubbles: the first close to the rotating shroud corner ($1.015 < r/r_{tip} < 1.035$ and $-0.15 < x/r_{tip} < -0.13$) and the second located close to the stationary casing one ($1.06 < r/r_{tip} < 1.12$ and $-0.14 < x/r_{tip} < -0.12$). Approaching the discharge section, the streamlines indicate that, in the $\Omega = 2400$ rev/min case, the leakage flow direction departs from the radial one with an increase in the axial component. Differently, in the $\Omega = 3000$ rev/min case, the leakage flow leaves the gap in the radial direction. This effect can be related with the different axial position of the rotating shroud in the two cases, but also different centrifugal effects may contribute. The $\bar{v}_\theta$ contour suggests that the mean tangential component in the leakage flow is generally larger for $\Omega = 2400$ rev/min than in the other regime. This is consistent with the findings of

Fig.7, since the leakage flow crosses the rotor but remains confined in the blade tip zone, hence maintaining a larger moment of momentum due to the lower mixing with the main flow. To this regard, it has to be taken in account that the flow inside the axial gap is subjected to an extremely high shear being one surface stationary and the other rotating at u_{tip} = 56.5 m/s or 70.2 m/s, with a radial gap equal to 5 mm. Then, assuming a linear trend of the tangential component, this leads to a radial gradient equal to 11 m/s per mm or 14 m/s per mm. Consequently, even slight variations of the flow trajectory between the two cases may lead to different moments of momentum in the leakage flow.

To further analyze this aspect, the local non-dimensional specific flux of moment of momentum $r/r_{tip}\overline{v_m v_\theta}$ has been computed and reported in Fig. 8. In the Ω =2400 rev/min case, the specific flux of moment of momentum in the leakage flow at the gap inlet is larger than for Ω =3000 rev/min, especially in the zone where a small separation bubble is present. While the leakage flow moves in upstream direction, the specific flux of moment of momentum appears to be conserved, until the inner wall of the rotating shroud is reached, where the viscous shear determines a local increase. This aspect is more effective in the Ω =2400 rev/min case.

The total non-dimensional flux of moment of momentum has then been computed in sections A and B according to the following equation:

$$G = \frac{1}{\rho\, A_{sec}} \int \rho\, r/r_{tip}\bar{v}_\theta\, \mathbf{v} \cdot \mathbf{n}\, dA \tag{1}$$

Table 1. The non-dimensional flux of moment of momentum G.

Operating point	Section A	Section B
Ω =2400 rev/min	5.88×10^{-4}	6.75×10^{-4}
Ω =3000 rev/min	3.76×10^{-4}	4.32×10^{-4}

In the two cases, in the outlet section G is 1.15 larger than in the inlet one, hence indicating a slight increase due to the shear determined by the spinning surface. Furthermore, for Ω =2400 rev/min, G is 1.56 larger than for Ω =3000 rev/min, but the leakage flow is directly reingested by the rotor. As a larger G is associated with a larger centrifugal force and hence to a stronger tendency of the flow towards the radial direction, such an aspect leads to exclude that the moment of momentum provides a major contribution to the different flow patterns.

In order to analyze the leakage flow periodicity inside the gap, the periodic meridional velocity component $\tilde{v}_m$ has been depicted in the whole gap region, see Fig. 9. In order to simplify the representation, the angular coordinate has been rectified and the entire shroud circumferential length is depicted. In the two cases, close to the gap inlet zone, $\tilde{v}_m$ is affected by $z_R = 9$ local maxima which have a spatial periodicity apparently related with the blade location. While the leakage flow evolves upstream, the maxima are partially attenuated, but still present. Consequently, even in the gap discharge section, the leakage flow is not released uniformly in θ direction, but (as suggested by the $\tilde{v}_m$ iso-surface) zones of larger $\tilde{v}_m$ are still present. The $\tilde{v}_\vartheta$ distributions confirm the different gap inlet conditions, as a matter of fact for Ω =2400 rev/min the flow entering the gap is characterized by larger $\tilde{v}_\vartheta$ values than in the Ω =3000 rev/min case in the region close to the upper casing where, as

indicated by the $\tilde{v}_m$ maxima, most of the fed inlet flow is concentrated. Such a characteristic confirms that in the Ω =2400 rev/min the leakage flow crosses the fan in a region close to the blade tip hence inducing a gap inlet flow characterized by larger $\tilde{v}_\vartheta$. Differently, in the Ω =3000 rev/min, the different leakage flow pattern acts in the way to reduce the tangential component at the fan inlet, consequently the flow entering the gap directly from the fan shows lower $\tilde{v}_\vartheta$ values. Such a feature is also present in the flow leaving the gap, hence confirming that the discrepancy in the leakage flow outlet direction cannot be ascribed to different centrifugal effects. The non-uniformity in θ direction reported for $\tilde{v}_m$ is also present in the $\tilde{v}_\vartheta$ distributions. Such non-uniformities, especially when developing in the gap discharge section, may induce the formation of the periodic coherent structures which have been identified in Fig. 6 together with non-periodic ones.
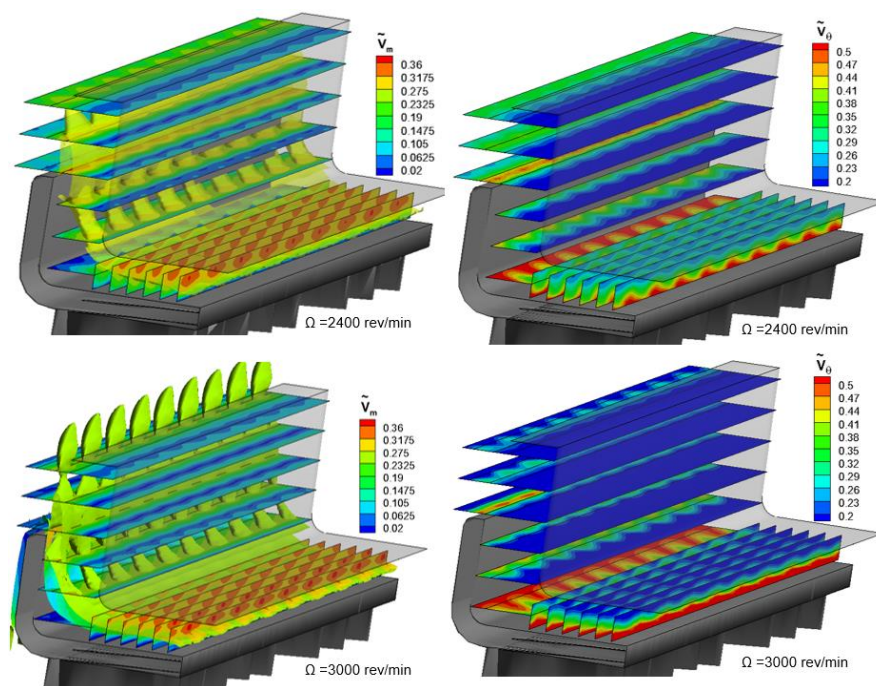

Figure 9: Periodic meridional and tangential velocity components contours in the gap zone with superposed iso-surfaces of the meridional velocity.

CONCLUSIONS

In the present work, a numerical investigation has been focused on the same geometry surveyed in previous experimental studies and starts on a fluid-structure interaction analysis developed through a one-way coupling method of CFD and FEM computations. The FEM analysis has been performed at five rotational speeds ranging from 500 to 3000 rev/min and same operating point, and the input pressure distributions on the rotor surfaces have been computed through steady CFD simulations on the design geometry. The achieved results are consistent with the experimental ones.

In the Ω =2400 rev/min and Ω =3000 rev/min cases, the deformed fan geometries have been used to perform detailed unsteady CFD simulations. The numerical results are in good agreement with the experimental ones. Although the non-dimensional flow rate and pressure coefficient have been kept

constant, depending on the rotational speed, two flow patterns that are consistent with the experimental ones have been observed in the gap region: at Ω =2400 rev/min, the leakage flow forms a recirculation bubble anchored to the rotating shroud and is quickly re-ingested by the fan. At Ω =3000 rev/min, it streams radially outwards and forms a large recirculation zone. The mean velocity components distributions in the gap region have allowed identifying the feeding mechanism of the leakage flow. Basically, two contributions may be identified: a highly swirling part that is directly sucked from the fan outlet while a second one is related with a separated flow characterized by a centripetal motion and lower values of the tangential component. While the non-dimensional leakage flow rate is independent of the rotational speed, 8.7% of the fan flow rate, the moment of momentum flux is larger in the Ω =2400 rev/min case. This aspect allows to exclude that the different leakage flow patterns may be ascribed to different centrifugal effects. Therefore, it may be inferred that the gap geometry modifications are the main cause of the pattern switch: if the axial displacement of the rotating shroud is sufficiently large, the leakage flow is able to stream radially out of the gap; differently it follows a more axial path and the suction induced by the fan becomes effective in determining a strong deflection. Besides, periodic flow features have been identified inside the gap region which yield a non-uniform velocity distribution in the gap discharge section at both rotational speeds.

REFERENCES

Canepa, E., Cattanei, A., Jafelice, F., Zecchin, F. M., & Parodi, D. (2018). Effect of rotor deformation and blade loading on the leakage noise in low-speed axial fans. Journal of Sound and Vibration, 433, 99-123.

Canepa, E., Cattanei, A., Mazzocut Zecchin, F., Milanese, G., Parodi, D., (2016). An experimental investigation on the tip leakage noise in axial-flow fans with rotating shroud. J. Sound Vib. 375, 115–131.

Canepa, E., Cattanei, A., Zecchin, F. M., & Parodi, D. (2019). Large-scale unsteady flow structures in the leakage flow of a low-speed axial fan with rotating shroud. Experimental Thermal and Fluid Science, 102, 1-19.

Corsini, A., Delibra, G., & Sheard, A. G. (2013). A critical review of computational methods and their application in industrial fan design. International Scholarly Research Notices, 2013.

Ghodake, D., Sanjosé, M., Moreau, S., & Henner, M., (2022). Effect of Sweep on Axial Fan Noise Sources Using the Lattice Boltzmann Method, International Journal of Turbomachinery Propulsion and Power 2022, 7(4), 34.

Gokpi, K., Marchesini, J., Demory, B., Henner, M., (2018), Turbo-machinery design based on multi-physics fluid-structure optimization, Fan 2018, Darmstadt, Germany.

Henner, M., Moreau, S., Brouckaert, J.F., (2009) Comparison of experimental and numerical flow field in an automotive engine cooling module, Proceedings 8th European Conference on Turbomachinery Fluid Dynamics and Thermodynamics (ETC'09), Graz, Austria, pp. 387e399.

Hussain, A. K. M. F., & Reynolds, W. C. (1970). The mechanics of an organized wave in turbulent shear flow. Journal of Fluid Mechanics, 41(2), 241-258.

Jasak, H., & Uroić, T. (2020). Practical computational fluid dynamics with the finite volume method. Modeling in Engineering Using Innovative Numerical Methods for Solids and Fluids, 103-161.

Longhouse, R., (1978), Control of tip-vortex noise of axial flow fans by rotating shrouds, J. Sound Vib. 58 (2) 201–214.

Magne, S., Sanjosé, M., Moreau, S. Berry, A., (2012), Aeroacoustics prediction of the tonal noise radiated by a ring fan in uniform inlet flow, Proceedings of the 33th AIAA Aeroacoustics Conference, AIAA-Paper2012-2122.

Magne, S., Moreau, S., Berry, A., (2015), Subharmonic tonal noise from back flow vortices radiated by a low-speed ring fan in uniform inlet flow, Journal of the Acoustical Society of America 137(1) 228–237.

Moreau, S., Boulanger, P., (2000), FEA computations applied to engine cooling fans, SAE International Congress and Exposition, SAE Technical Papers 2000- 01-0968, Detroit, MI.

Moreau, S., Henner, M., Casalino, D., Gullbrand, J., Iaccarino, G., & Wang, M. (2006). Toward the prediction of low-speed fan noise. In Proceedings of the summer program (Vol. 9). Center for Turbulence Research.

Moreau, S., Sanjose, M., (2016), Sub-harmonic broadband humps and tip noise in low-speed ring fans, Journal of the Acoustical Society of America 139(1), 118–127.

Nouri, H., Ravelet, F., Sarraf, C., Bakir, F., (2010), Experimental study of blade rigidity effects on the global and the local performances of a thick blades axial-flow fan, American Society of Mechanical Engineers, Fluids Engineering Division (Publication) FEDSM, 1 (PARTS A, B and C), pp. 671e678.

Piellard, M., Coutty, B., Le Goff, V., Vidal, V., Pérot, F., (2014), Direct aeroacoustics simulation of automotive engine cooling fan system: effect of upstream geometry on broadband noise, 20th AIAA /CEAS Aeroacoustics Conference, AIAA Paper 2014-2455, Atlanta, Georgia.

Romik, D., & Czajka, I. (2022). Numerical Investigation of the Sensitivity of the Acoustic Power Level to Changes in Selected Design Parameters of an Axial Fan. Energies, 15(4), 1357.

Zayani, M., Çağlar, Ş. , Gabi, M., (2012), Aero acoustical investigations on skewed axial fans for automotive cooling systems, Proceedings of the 41st International Congress and Exposition on Noise Control Engineering 2012, INTER-NOISE 2012, Vol.10, pp.8077–8088.

Zhu, M., Wang, K., Zhang, P., & Li, Z. (2015). Numerical and experimental investigation of aerodynamic noise from automotive cooling fan module. Journal of Vibroengineering, 17(2), 967-977.